

Intrinsic Catalytic Activity of Graphene Defects for the $\text{Co}^{\text{II/III}}(\text{bpy})_3$ Dye-Sensitized Solar Cell Redox Mediator

Joseph D. Roy-Mayhew,^{†,§} Michael A. Pope,^{†,‡,||} Christian Punckt,^{†,‡,⊥} and Ilhan A. Aksay^{*,†}

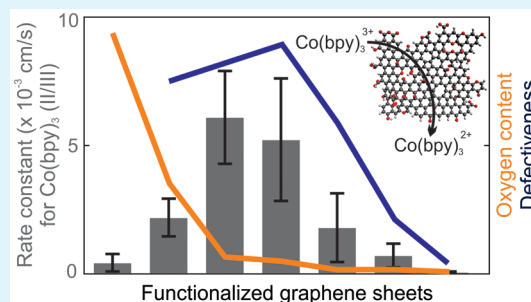
[†]Department of Chemical and Biological Engineering, Princeton University, Princeton, New Jersey 08544, United States

[‡]Vorbeck Princeton Research Center, Vorbeck Materials Corporation, 11 Deerpark Drive, Suite 203, Monmouth Junction, New Jersey 08852, United States

Supporting Information

ABSTRACT: We demonstrate that functionalized graphene, rich with lattice defects but lean with oxygen sites, catalyzes the reduction of $\text{Co}^{\text{III}}(\text{bpy})_3$ as well as platinum does, exhibiting a rate of heterogeneous electron transfer, k_0 , of $\sim 6 \times 10^{-3}$ cm/s. We show this rate to be an order of magnitude higher than on oxygen-site-rich graphene oxide, and over 2 orders of magnitude higher than on the basal plane of graphite (as a surrogate for pristine graphene). Furthermore, dye-sensitized solar cells using defect-rich graphene monolayers perform similarly to those using platinum nanoparticles as the catalyst.

KEYWORDS: graphene, dye-sensitized solar cell, catalytic activity, rate constant, heterogeneous electron transfer, cobalt redox mediator, electrocatalysis



INTRODUCTION

Dye-sensitized solar cells (DSSCs) have been touted as potential low-cost clean energy harvesting devices.¹ Typically, they use a high surface area semiconductor scaffold sensitized with dye molecules as the photoanode, a redox couple dissolved in a suitable electrolyte to transport electrons from the cathode to the dye, and a catalytic counter electrode as the cathode, which regenerates the redox couple.² While platinum nanoparticles, produced through the thermal decomposition of chloroplatinic acid,³ have been the dominant counter electrode catalyst, many studies have investigated alternatives to this precious metal. Particularly promising catalysts include transition-metal compounds (e.g., CoS, VC, and TiN),^{4,5} conductive polymers,⁶ and carbonaceous nanomaterials such as carbon black,^{7,8} carbon nanotubes,^{9,10} and reduced graphene oxide.^{11–16}

Carbonaceous materials are capable of matching or even exceeding the performance of platinum electrodes for a variety of redox mediators, but the sites that are responsible for catalysis have not yet been identified.^{15–18} Some studies, including our own, have hypothesized that oxygen functionalities may be the primary agents of catalysis,^{10,11,19} while others suggest dangling bonds at lattice vacancies and edges as the catalytic sites.^{15,20} While the apparent electrochemical activity of a catalyst can be determined through cyclic voltammetry and electrochemical impedance spectroscopy (EIS),²¹ the intrinsic activity of a material, particularly high surface area carbonaceous materials, is obfuscated by morphology. Both theoretical and experimental studies have shown that porosity can increase the peak current (I_p) and decrease the peak-to-peak separation (E_{pp}) in cyclic voltammograms (CVs) and thus affect the extracted electro-

chemical parameters.^{22–24} Furthermore, the high electronic resistance that exists in networks of poorly conducting particles (i.e., graphene oxide) can decrease or even eliminate the observed catalytic activity of a material.

Herein, using cyclic voltammetry and EIS, we test monolayers of graphene oxide and its reduced forms (hereafter referred to as functionalized graphene sheets, FGSs) to determine the intrinsic catalytic activity of oxygen functional groups and lattice defect sites toward the $\text{Co}^{\text{II/III}}(\text{bpy})_3$ redox system, where $\text{bpy} = 2,2'$ -bipyridine. We differentiate between FGSs on the basis of oxygen content through the nomenclature FGS_{*x*}, where *x* represents the molar carbon to oxygen ratio (C/O). In addition to being the electrolyte in a previous record-efficiency DSSC,²⁵ the cobalt mediator was chosen for the present study because the complex involves a single electron transfer, unlike the common iodide–triiodide mediator. This simplicity facilitates a clear interpretation of electrochemical data and assessment of catalytic activity.

RESULTS AND DISCUSSION

As shown by the scanning electron microscopy (SEM) images of Figure 1, by using a Langmuir–Blodgett (LB) trough approach, wherein we adsorb dispersed sheets at the air–water interface and compress them into a densely packed film,^{26–31} we form patchwork monolayers of FGSs with negligible roughness. The relative coverage of these films, estimated by SEM, ranges from 85% to 95%. In Figure 2, we show two complementary

Received: January 23, 2016

Accepted: March 21, 2016

Published: March 21, 2016

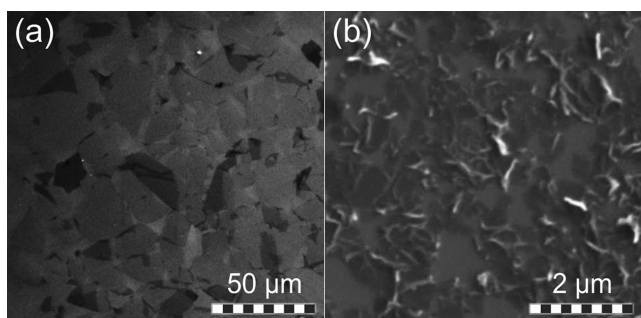


Figure 1. SEM images of (a) FGS₂ and (b) FGS₆₈ layers on silicon. Silicon substrates (lightest regions) are shown as they provide greater contrast with the darker FGSs. The surface coverage for these examples is greater than 90%, and a few instances of overlapping sheets are observed.

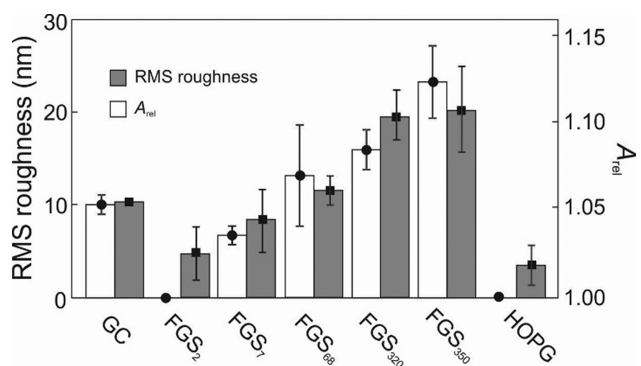


Figure 2. RMS roughness and A_{rel} of various electrodes used in this study determined by AFM. Error bars were estimated using the standard deviation of five randomly chosen $5 \mu\text{m} \times 5 \mu\text{m}$ scan areas. A_{rel} for FGS₂ and HOPG was not exactly unity but ~ 1.0002 , as these surfaces are nearly atomically flat but do contain steps and ledges. These steps and ledges contribute more to the RMS roughness than A_{rel} .

characteristics of the film morphology, the root-mean-square (RMS) roughness and the ratio of the true to projected area, A_{rel} (i.e., the relative surface area increase) as determined by atomic force microscopy (AFM). These values provide information about the height of the roughness features as well as the degree to which these features contribute to an increase of the effective electrochemically active surface area of the electrode. The RMS roughness rises with increasing temperature of thermal treatment up to about 20 nm (see Figure 2). This result arises from the wrinkled and partly folded morphology, which can be caused by overlapping or folding during the film deposition process and by the thermal expansion and annealing process, which is known to result in FGSs with such wrinkled features.^{32,33} As a result, the true surface area of the films is slightly higher than the projected area. We obtain values of $A_{rel} = 1.0002$ for FGS₂ (i.e., graphene oxide) and values ranging between $A_{rel} = 1.03$ and $A_{rel} = 1.13$ for FGSs produced by thermal expansion of graphite oxide, as shown in Figure 2, which are on the same order as what we measure for typical polished glassy carbon (GC) electrodes ($A_{rel} = 1.05$). The fact that the RMS roughness and A_{rel} are correlated for the thermally exfoliated materials suggests that the lateral feature size is fairly constant; i.e., morphological features such as wrinkles exhibit similar average lateral separation between samples but have increasing height. On the other hand, the FGS₂ and highly oriented pyrolytic graphite (HOPG) samples, which are nearly atomically flat and have roughness mainly emanating from

infrequent steps and ledges with large lateral separation, display A_{rel} values approaching 1 (~ 1.0002) but still have finite values of RMS roughness. Taking into account the relative coverage and effective surface areas, we conclude that each of our FGS films behaves as a continuous flat electrode, as the nanometer-scale inhomogeneities in the monolayers resulting from roughness and the effective distance between sheets are much smaller than the diffusion length of the redox probe ($>19 \mu\text{m}$ in our experiments; see the Supporting Information for diffusion coefficient determination). Through this approach, we thus reduce the effect of the morphology to a negligible range, as demonstrated previously.^{28,29,31} Additionally, electronic losses, especially important with insulating FGS₂ films, are minimized due to the mosaic of single layer sheets in direct contact with the conducting substrates.

To determine the catalytic role of oxygen groups, we varied their presence on the sheets over 2 orders of magnitude through thermal treatment, as measured by C/O (from ~ 0 to 33 atom % oxygen), as seen in Figure 3. The basal plane of HOPG is used as

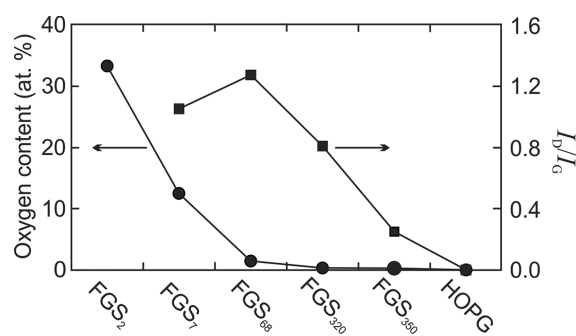


Figure 3. FGS_x oxygen content (●) and defectiveness as measured by I_D/I_G of Raman data (see the text) (■). Oxygen content calculations do not take into account the contribution of hydrogen. I_D/I_G data are from ref 31.

a surrogate for pristine graphene ($C/O \rightarrow \infty$). Although the oxygen content is a convenient identifier, it is not a unique one, as for a given value of C/O there can be different compositions of oxygen groups (epoxides, hydroxyls, carbonyls, etc.)^{34,35} and lattice defects (topological defects, lattice vacancies, etc.) on the sheets,^{34,36,37} which can affect the chemical and electrical properties of the material.

Thermal treatment of FGS₂ removes oxygen from the material through the evolution of CO, CO₂, H₂O, and O₂, leaving behind lattice defect sites when carbon is removed from the lattice.^{32,33,38,39} However, at elevated temperatures, as the lattice diffusion rate of carbon is enhanced, the lattice defects can heal,⁴⁰ and the structure moves toward a more pristine graphene state. To infer how these processes affect the structure of FGSs after various reduction and annealing procedures, we used Raman spectroscopy to follow the peak intensities, peak positions, and peak widths of the G- and D-bands. The G-band arises due to vibrations of pairs of sp^2 -bonded carbon atoms, and thus, its intensity scales with the number of sp^2 -bonded carbon atoms in the material. The D-band, on the other hand, is due to the breathing oscillation of aromatic six-membered rings of carbon atoms, and its intensity scales with the number of edge-site dangling bonds, functional groups, and lattice defects whose presence and distribution define the lateral crystallite size of pristine graphene domains (L_A) within the material.^{41,42}

The D-band shows nonmonotonic behavior because the intensity grows with the number of six-membered aromatic rings, but the oscillation is dampened when L_A exceeds ~ 2 nm.⁴³ A more systematic analysis of FGSs annealed over a larger number of temperatures was recently published,³¹ and we reproduce several of the results corresponding to the materials used in this study in Figures 3 and 4.

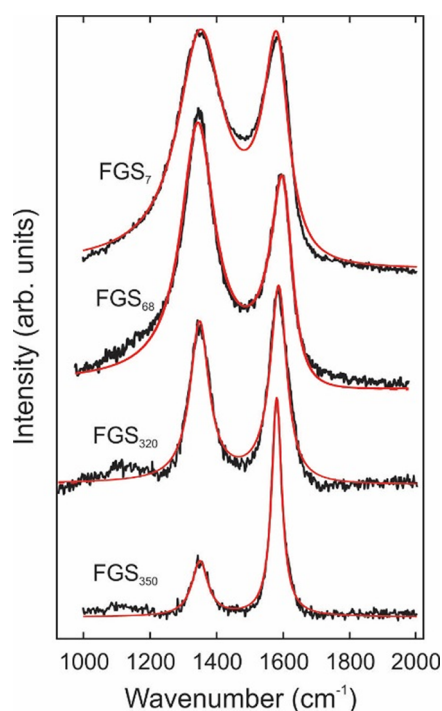


Figure 4. Raw Raman data (black) and calculated fit (red) of FGSs used to determine I_D/I_G . This approach is expanded further in ref 31.

Figure 3 shows that the I_D/I_G ratio increases from FGS₇ to FGS₆₈ and then decreases for materials heat treated at higher temperatures (FGS₃₂₀ and FGS₃₅₀). As shown in Figure 4, there is a significant narrowing of the full width at half-maximum (fwhm) between FGS₇ and FGS₆₈. This indicates that a significant number of defects remains in FGS₆₈, but the distribution of defect types becomes narrower.⁴³ The removal of functional groups, which can be considered defects between pristine graphene domains, likely explains this change, while lattice defects in the form of reconstructed vacancies or structural defects remain and maintain a high I_D/I_G . Annealing at higher temperatures (>1300 °C) causes further narrowing of both the D- and G-peaks and a decrease in the I_D/I_G that can be explained by the healing of lattice defects and the growth of pristine graphene domains (i.e., an increase in L_A).

CVs in Figure 5 show that C/O of a material has a profound effect on the intrinsic catalytic activity for the $\text{Co}^{\text{II/III}}(\text{bpy})_3$ redox couple. As C/O increases, the catalytic activity (as indicated by E_{pp} and I_p) first increases and then decreases.^{21,23} HOPG shows no appreciable rate of electron transfer in this voltage window, consistent with previous reports for the low activity of HOPG.^{15,17,44} FGS₂ performs significantly better than HOPG, building upon the work of Kavan et al.¹⁵ That study maintained similar activity between the materials, although a slight advantage was seen in the oxidized material via EIS. The electrodes used in their work were formed through drop casting, spin coating, and airbrush coating, all techniques that form films of multiple layers.

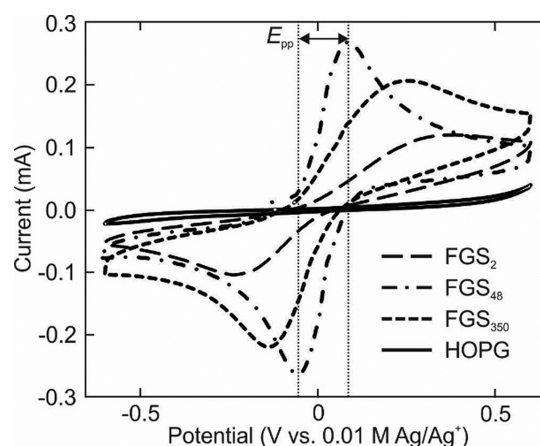


Figure 5. CVs of the $\text{Co}^{\text{II/III}}(\text{bpy})_3$ redox couple, 1 mM, with FGS_x monolayer electrodes. The scan rate is 1 V/s.

FGS₂ films, even a few nanometers thick, prevent electron transfer due to the insulating properties of the material. Our own attempts to make FGS₂ multilayers on conductive substrates using drop casting and spin coating techniques also resulted in inactive electrodes (data not shown), thus motivating our use of LB monolayer electrodes.

An overview of the dependence of the catalytic activity on the degree of FGS reduction is provided in Figure 6, where we

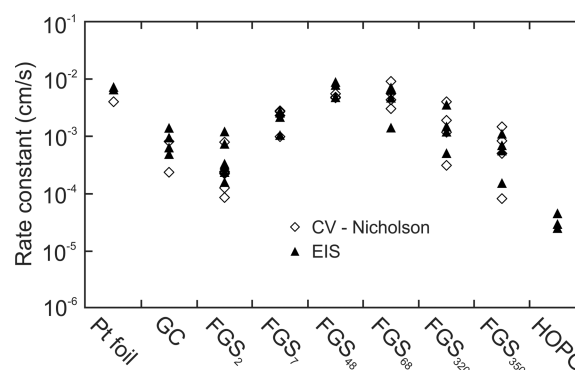


Figure 6. Reaction rate constants for the $\text{Co}^{\text{II/III}}(\text{bpy})_3$ redox couple. FGS_x monolayers were tested on both HOPG and fluorine-doped tin oxide substrates.

compare the heterogeneous electron transfer (HET) rate k_0 determined for different types of FGSs with that measured on polished platinum, GC, and HOPG. To determine k_0 , CVs were analyzed by employing Nicholson's method as described in Bard's foundational text.²¹ Two additional techniques are used to further support these findings (details for all three methods can be found in the Supporting Information). EIS data were fit to an equivalent circuit model to determine the charge transfer resistance and, from this, the HET rate.²¹ For samples where peaks are not present in the CV scan window (e.g., HOPG samples), we reinforced our EIS results with Tafel slope analysis (data not shown). These three different approaches for the determination of k_0 yielded results that were in agreement for any given sample.

Rate constants measured with FGS₂ are over 10 times larger than those measured with HOPG, supporting the claim that oxygen functional groups act as catalytic sites on FGSs and, by extension, on other carbonaceous materials. Nevertheless,

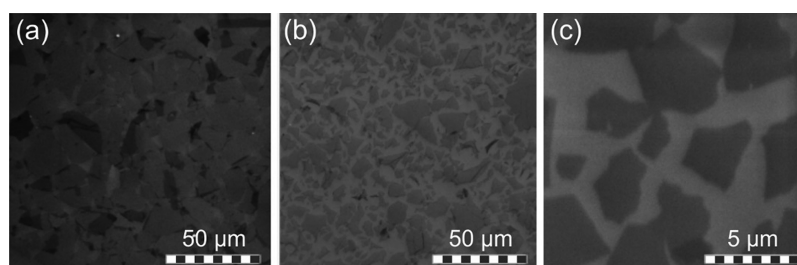


Figure 7. SEM images of FGS₂ monolayers: large, $\sim 200\ \mu\text{m}$ (a), and small, $\sim 20\ \mu\text{m}$ (b, c), sheet monolayers used in electrochemical measurements.

thermally reducing FGS₂ improves the reaction rate further. In fact, FGS₆₈ and its industrially produced counterpart, FGS₄₈ (Vorbeck Materials Corp.), have activities that match that of platinum ($k_0 \approx 6 \times 10^{-3}\ \text{cm/s}$). Additional thermal treatment above $1100\ ^\circ\text{C}$ decreases activity, correlating with a decrease in FGS defectiveness.

The observations from Figure 6 support the interpretation that lattice defects are highly active, while oxygen sites and pristine graphene domains are moderately and poorly active, respectively. As moderately active oxygen sites on FGS₂ are thermally reduced, CO₂ and CO are evolved, removing carbon atoms from the lattice. This process results in vacancies or other highly active defect sites which improve the overall activity of the material.^{31–34,37,38} At high temperatures, the lattice defects can migrate and are effectively replaced by pristine graphene domains,^{31,40} thereby reducing the activity. The maximum in lattice defect concentration at FGS₆₈ in Figure 3, indicated by the maximum in the I_D/I_G ratio, corresponds to a maximum in the rate constant in Figure 6. This study does not distinguish which lattice defect sites are most active; however, the literature suggests some to be relatively inert (i.e., Stone–Wales, 5–7–7–5, and structural defects) and some to be more active (i.e., carbon vacancies).^{45,46} We also acknowledge that specific oxygen sites likely have different activities as well, and a small number of highly active oxygen sites may be responsible for the perceived activity of oxygen-rich FGS. Additionally, some oxygen sites can be created during the reduction process,^{37,39} and we cannot rule out the possibility that these sites are highly active and responsible for the increased activity. Lastly, it is possible that the lattice defects have associated oxygen groups which are responsible for increased activity.⁴⁵

While we did not determine the specific type of oxygen sites (e.g., epoxide, carbonyl, etc.) contained on the FGSs as a function of reduction and annealing conditions, we were able to probe the activity of edge versus surface (i.e., basal plane) oxygen sites through two indirect methods: (1) by varying the sheet size and thus the number density of edge sites and (2) by using GC as a proxy material. If edge sites had superior activity, we would expect samples with a larger number of these sites to exhibit greater activity. For a set sample area (in our case $1\ \text{cm}^2$) monolayers made up of smaller sheets would have more edge sites as the perimeter to area ratio is larger. Nevertheless, samples from large ($\sim 200\ \mu\text{m}^2$) and small ($\sim 20\ \mu\text{m}^2$) sheets behave similarly in electrochemical measurements and, correcting for area coverage, exhibit statistically equivalent performance. The rate constant for large FGS₂ samples is $2.5 \times 10^{-4}\ \text{cm/s}$, and that for small FGS₂ samples is $1.6 \times 10^{-4}\ \text{cm/s}$ (sample sizes of 10 and 8, respectively). Accounting for surface coverage, the rate constant for small FGS₂ samples is $2.5 \times 10^{-4}\ \text{cm/s}$. Large sheets of FGS₂ were primarily used in this study due to the ease in forming monolayers from this material.²⁷ Large sheets float more

readily at the air–water interface. Smaller sheets, which can be obtained by sonicating suspensions of larger FGS₂ sheets, tend to sink into the water phase of the LB trough, and much more material must be used to obtain an acceptable monolayer. Examples of the two different monolayers are shown in Figure 7. Drop casting and spin coating techniques were also attempted to form a monolayer of smaller sheets; however, large-area ($1\ \text{cm}^2$) uniformity could not be achieved.

Furthermore, oxidized GC, whose structure is proposed to have a high proportion of edge atoms with oxygen functional groups, had activity similar to that of untreated GC.^{47,48} These results, in agreement with the above, suggest that sheet edges, with their carbonyl and other oxygen functional groups,⁴⁹ may not be the dominant reactive site for the cobalt mediator, as is often suggested for other systems.^{50,51} In other words, since we do not observe a correlation between a high number density of oxygen functional groups and high catalytic activity, we conclude that those types of functional groups present on FGS₂ and oxygen plasma-treated GC show significantly weaker catalytic activity than lattice defects (with or without associated oxygen).

To further support the results of Figure 6, we also studied another route to varying the properties of FGS monolayers using films with the same initial morphology. To achieve this, FGS₂ monolayers were transferred to fluorine-doped tin oxide substrates and then heated in air to 150, 250, and 350 $^\circ\text{C}$, resulting in FGSs with C/O of 2.9, 4.5, and 6.9, as estimated from the heating of bulk powder and subsequent measurement by energy-dispersive X-ray spectroscopy. A trend of increasing activity was observed, with the data falling between the results from FGS₂ and FGS₄₈ samples ($k_0 \approx 0.7 \times 10^{-3}$, 2.4×10^{-3} , and $3.5 \times 10^{-3}\ \text{cm/s}$, respectively). As the samples matched or outperformed FGS₇ at lower C/O, the partial thermolysis of the material in the presence of oxygen may have increased the density of catalytic lattice defect sites.

We also electrochemically reduced FGS₂ monolayers in situ, a technique that is suggested to remove oxygen without disrupting the carbon lattice.⁵² This was carried out both in aqueous (as detailed by Zhou et al.⁵²) and in acetonitrile-based electrolytes by applying sufficiently negative potentials to the electrode (see the Supporting Information). Unlike thermal reduction, electrochemical reduction resulted in a material with decreased activity compared to FGS₂ ($k_0 \approx 1.7 \times 10^{-4}\ \text{cm/s}$), which is consistent with it losing active oxygen functionalities and yielding a less defective form of graphene. No change in FGS₂ activity was observed after scanning in our normal scan window (-0.6 to $+0.6\ \text{V vs Ag/Ag}^+$); however, at mild reduction conditions (scan to $-0.8\ \text{V vs Ag/Ag}^+$), the activity increased almost 100%, before declining at higher degrees of reduction (see the Supporting Information for details). This result could be explained by the trade-off between the increase of conductivity, which facilitates

electron transfer, and the loss of active sites, both due to the removal of oxygen groups.

DSSCs similar to those employed by Feldt et al.⁵³ were fabricated using the cobalt mediator, D35 dye, and the various counter electrodes. The current density–voltage curves shown in Figure 8 support the cyclic voltammetry and EIS findings, with

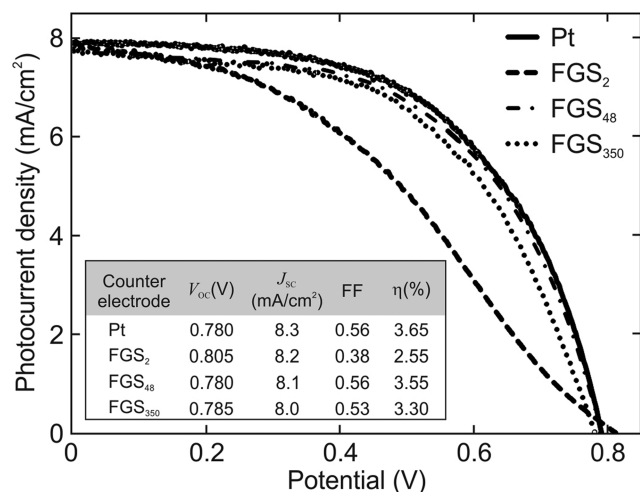


Figure 8. Current density–voltage curves for DSSCs using thermalized chloroplatinic acid (Pt) and FGS_x monolayer counter electrodes. The inset shows average device characteristics measured for three cells. Cells were characterized under AM 1.5G (1000 W/m²) illumination. V_{OC} is the open circuit voltage, J_{SC} is the short circuit current, FF is the fill factor, and η is the power conversion efficiency. The active area is 0.25 cm².

FGS₄₈ performing similarly to platinum, followed by FGS₃₅₀ and FGS₂. Of note, here thermalized platinum acid is used as it has been shown to form nanoscale platinum clusters, ~5 nm in diameter, which have higher surface area and activity ($k_0 \approx 2 \times 10^{-2}$ cm/s) than the metal's planar counterpart.³ Due to the higher concentration of the cobalt mediator in the DSSC, a charge transfer resistance of 1 Ω can be achieved at the cathode with a reduction rate constant of 8×10^{-3} cm/s. Thus, a faster reaction rate than what we achieve with FGS₄₈ samples has little advantage in a device, as is seen. The high charge transfer resistance from low catalytic activity is noticeable, however, in the poor fill factor of the FGS₂ device.

CONCLUSION

Using tunable FGS monolayers, we determined the relative efficacy of various functional sites on defective graphene toward the Co^{II/III}(bpy)₃ mediator. The basal plane of HOPG, as a surrogate for pristine graphene, shows low activity ($k_0 \approx 2.7 \times 10^{-5}$ cm/s), while FGS₄₈ with a high lattice disorder and low oxygen content shows ~220 times greater activity. The relative performance is conserved in DSSCs: Cells using a single layer of FGS₄₈ as the catalyst perform as well as those using thermalized platinum acid. This work represents an important step forward in understanding carbonaceous materials by determining the intrinsic catalytic activity of FGSs with different oxygen contents and degrees of defectiveness.

MATERIALS AND METHODS

Unless otherwise stated, all chemicals used were electrochemical grade from Sigma-Aldrich and were used as received. Water used was deionized with a resistivity of about 18 M Ω -cm.

Preparation of FGS_x. FGSs were prepared as described by Pope et al.⁵⁴ To synthesize FGS₂, a modified Hummers method⁵⁵ was carried out according to the procedure of Cote et al.²⁷ In short, with continuous stirring in an ice bath, a slurry of 0.5 g of graphite (Asbury grade 3061), 0.5 g of NaNO₃, and 23 mL of H₂SO₄ was prepared. Subsequently, 3 g of KMnO₄ was added, and the slurry was heated to 35 °C and stirred for 1 h. A 400 mL volume of water was then added, and the resulting suspension was stirred for 30 min, during which time the reaction temperature was increased to ~90 °C. Still under stirring, 100 mL of water was then added, followed by 3 mL of H₂O₂ (30%). Centrifugation was used to separate FGS₂ from the soluble components of the reaction mixture and also to select for large sheets that float at the air–water interface more easily.^{27,56} Reduced FGS₂ was produced by a thermal exfoliation and, for C/O > 100 materials, a subsequent annealing step was used. Thermal exfoliation took place in a tube furnace (Blue M, SPX Thermal Products) at temperatures between 300 °C (FGS₇) and 1100 °C (FGS₆₈) under argon. Annealing consisted of heating thermally exfoliated powder for 2 h in a resistively heated graphite furnace (Astro-1000, Thermal Technologies) at 1300 °C (FGS₃₂₀) and 1900 °C (FGS₃₅₀) under argon. FGS₄₈ was generously provided by Vorbeck Materials Corp. (batch RC123).

Preparation of Monolayers. Monolayers were prepared similarly to those in previous work.²⁸ In brief, aqueous suspensions of FGS₂ were mixed with methanol (Fisher) at a 1:5 volume ratio. FGSs with C/O of 7 and above were suspended in residue-free 1,2-dichloroethane (Acros) at a concentration of 5 mg/15 mL, and the resulting suspensions were tip sonicated (150 W, Branson Ultrasonics) for 30 min at 40% amplitude in an ice bath. Aggregates were removed by centrifugation at 2000g for 60 min. The suspensions were spread out on the air–water interface of an LB trough (Nima Technology) using a syringe pump set at a flow rate of 0.2 mL/min. A sufficient coverage of FGSs was attained after the addition of 0.5–3 mL of suspension. The FGS₂ coverage was observed with a Brewster angle microscope (BAM2plus, Nanofilm Technologie GmbH), and the surface tension was monitored using a Wilhelmy plate cut from filter paper. LB films of reduced FGSs could be observed by the eye as a faint film. Movable Teflon barriers were used to densify the film by reducing the area at a rate of 20 cm²/min. The LB films were transferred to HOPG (freshly cleaved, grade 2, Structure Probe), fluorine-doped tin oxide (FTO; TEC 8, Hartford Glass), and silicon (from a 4 in. 100 test grade wafer) by the horizontal deposition method.⁵⁷ In this method, the substrates were placed in the water subphase in the absence of the LB film. Once the LB film was under compression, it was lowered onto the various surfaces by removing water from the trough. Coated samples were air-dried for 10 min and then placed on a hot plate at 80 °C until use. The processing conditions for the samples used in this work are tabulated in Table 1, including

Table 1. Material Processing Conditions

| sample name | conditions |
|--------------------|--|
| Pt foil | polished |
| GC | polished, oxygen plasma for 5 min at 500 mTorr |
| FGS ₂ | ultrasonic exfoliation of GO in ammoniated water (pH 10) |
| FGS ₇ | exfoliation of GO at 300 °C for 60 s |
| FGS ₄₈ | Vor-x, supplied by Vorbeck Materials Corp. |
| FGS ₆₈ | exfoliation of GO at 1100 °C for 300 s |
| FGS ₃₂₀ | exfoliation of GO at 1100 °C for 60 s, annealed at 1300 °C for 2 h |
| FGS ₃₅₀ | exfoliation of GO at 1100 °C for 60 s, annealed at 1900 °C for 2 h |
| HOPG | freshly cleaved |

preparation conditions for three reference materials (polished platinum, GC, and HOPG) used for comparison. FGS materials were prepared through exfoliation of graphite oxide (GO).

Preparation of Dye-Sensitized Solar Cells. DSSCs were constructed as described previously in the literature.¹² FTO glass (TEC15, Hartford Glass) was cleaned in an ultrasonic bath overnight in ethanol (Fisher). A TiO₂ underlayer was formed by pretreating the glass at 70 °C in a 40 mM TiCl₄ solution for 30 min. The films were then

subsequently washed with water and ethanol. TiO₂ films, 0.5 × 0.5 cm², were prepared by screen printing two layers of a colloidal TiO₂ paste (Dyesol DSL 18 NR-T). Two layers of a scattering paste (PST-400C, JGS Catalysts and Chemicals) were then screen printed on top of the TiO₂ nanoparticle film. The resulting films had a thickness of ~18 μm. The electrodes were heated (Nabertherm Controller P320) in an air atmosphere at 180 °C (10 min), 320 °C (10 min), 390 °C (10 min), and 500 °C (30 min). A final TiCl₄ treatment was performed similar to that above, and the electrodes were sintered again using the above protocol. Before use, the electrodes were heated to 300 °C to remove water, and allowed to cool to 80 °C, at which temperature they were placed in a dye solution (0.2 mM D35 dye in ethanol) overnight. The films were then rinsed with ethanol and dried. Platinum counter electrodes were prepared by depositing a 4.8 mM chloroplatinic acid solution in ethanol onto the FTO glass substrate (10 μL/cm²) and then heating the electrode to 400 °C for 30 min before use. FGS_x counter electrodes were prepared by depositing an LB monolayer onto the FTO glass substrate, as described above. Electrolyte (0.22 M Co(bpy)₃(PF₆)₂, 0.033 M Co(bpy)₃(PF₆)₂, 0.1 M LiClO₄, and 0.2 M 4-*tert*-butylpyridine in acetonitrile) was added via vacuum filling through holes in the counter electrode. A 50 μm Surlyn thermoplastic film was used to separate the photoanode and the counter electrode and to seal the cell after electrolyte was added.

Characterization (SEM, EDS). Electrodes were characterized by SEM (VEGAI, Tescan USA) at a 20 kV acceleration voltage. C/O of FGS powder was determined through energy-dispersive X-ray spectroscopy (INCA x-act, Oxford Instruments) at a 10 kV accelerating voltage and confirmed with combustion-based analysis.

Measurements. Cyclic voltammetry, EIS, and solar cell characterization were performed using a Biologic SP-150 potentiostat. CVs were taken from 5 to 1000 mV/s, and data were analyzed with a customized Matlab code. The solution resistance was measured before cyclic voltammetry tests and compensated for during the measurements. EIS measurements were taken at 0 V, the magnitude of the alternating signal was 10 mV, and the frequency range was 1 Hz to 100 kHz. ZFit (Biologic) and a customized Matlab code were used to analyze the impedance spectra. For measurements, a homemade electrochemical cell was designed to hold block-type electrodes as described by Pope et al.²⁸ This device is a slightly modified version of the electrode holder described by Randin and Yeager⁵⁸ and later modified by Compton's group.⁵⁹ The electrodes are spring-loaded against an O-ring that is used to isolate the electrochemically active surface area. The screw-on Teflon lid features ports for a platinum wire counter electrode, a Ag/Ag⁺ (0.01 M AgNO₃, 0.1 M LiClO₄) reference electrode, and a Teflon hose for nitrogen purging. Current–voltage characteristics of DSSCs were taken under AM1.5G light, simulated at 1000 W/m² using a 16S solar simulator (SolarLight) calibrated with a PMA2144 pyranometer (SolarLight). Data values presented are the average of three identically prepared samples, while figures are representative of individual runs.

■ ASSOCIATED CONTENT

Supporting Information

The Supporting Information is available free of charge on the ACS Publications website at DOI: 10.1021/acsami.6b00937.

Sample roughness AFM images, rate constant and diffusion coefficient determination, and electrochemical reduction of FGS₂ (PDF)

■ AUTHOR INFORMATION

Corresponding Author

*E-mail: iaksay@princeton.edu.

Present Addresses

§J.D.R.-M.: Deloitte, 200 Berkeley St., Boston, MA 02116.

||M.A.P.: University of Waterloo, 200 University Ave. W., Waterloo, ON N2L 3G1, Canada.

†C.P.: Karlsruhe Institute of Technology, Institute of Nanotechnology, Hermann-von-Helmholtz-Platz 1, 76344 Eggenstein-Leopoldshafen, Germany.

Notes

The authors declare the following competing financial interest(s): The authors declare financial interest in Vorbeck Materials Corp., which manufactures FGSs under the trade name Vor-x.

■ ACKNOWLEDGMENTS

We thank P. Lohse (Uppsala University) for supplying the cobalt redox mediator, G. Boschloo and A. Hagfeldt (Uppsala University) for supplying the D35 dye, and J. S. Lettow (Vorbeck Materials Corp.) for supplying FGS₄₈. J.D.R.-M. was supported by a National Science Foundation Graduate Research Fellowship under Grant No. DGE-0646086. This work was supported by the Pacific Northwest National Laboratory (operated for the United States Department of Energy by Battelle) through Battelle Grant No. 66354.

■ REFERENCES

- (1) O'Regan, B.; Grätzel, M. A Low-Cost, High-Efficiency Solar Cell Based on Dye-Sensitized Colloidal TiO₂ Films. *Nature* **1991**, *353*, 737–740.
- (2) Hagfeldt, A.; Boschloo, G.; Sun, L.; Pettersson, H. Dye-Sensitized Solar Cells. *Chem. Rev.* **2010**, *110*, 6595–6663.
- (3) Papageorgiou, N.; Maier, W. F.; Grätzel, M. An Iodine/Triiodide Reduction Electrocatalyst for Aqueous and Organic Media. *J. Electrochem. Soc.* **1997**, *144*, 876–884.
- (4) Wang, M.; Anghel, A. M.; Marsan, B.; Cevey Ha, N.-L.; Pootrakulchote, N.; Zakeeruddin, S. M.; Grätzel, M. CoS Supersedes Pt as Efficient Electrocatalyst for Triiodide Reduction in Dye-Sensitized Solar Cells. *J. Am. Chem. Soc.* **2009**, *131*, 15976–15977.
- (5) Wu, M.; Lin, X.; Wang, Y.; Wang, L.; Guo, W.; Qi, D.; Peng, X.; Hagfeldt, A.; Grätzel, M.; Ma, T. Economical Pt-Free Catalysts for Counter Electrodes of Dye-Sensitized Solar Cells. *J. Am. Chem. Soc.* **2012**, *134*, 3419–3428.
- (6) Ahmad, S.; Yum, J.-H.; Butt, H.-J.; Nazeeruddin, M. K.; Grätzel, M. Efficient Platinum-Free Counter Electrodes for Dye-Sensitized Solar Cell Applications. *ChemPhysChem* **2010**, *11*, 2814–2819.
- (7) Kay, A.; Grätzel, M. Low Cost Photovoltaic Modules Based on Dye Sensitized Nanocrystalline Titanium Dioxide and Carbon Powder. *Sol. Energy Mater. Sol. Cells* **1996**, *44*, 99–117.
- (8) Murakami, T. N.; Ito, S.; Wang, Q.; Nazeeruddin, M. K.; Bessho, T.; Cesar, I.; Liska, P.; Humphry-Baker, R.; Comte, P.; Pechy, P.; Grätzel, M. Highly Efficient Dye-Sensitized Solar Cells Based on Carbon Black Counter Electrodes. *J. Electrochem. Soc.* **2006**, *153*, A2255–A2261.
- (9) Suzuki, K.; Yamaguchi, M.; Kumagai, M.; Yanagida, S. Application of Carbon Nanotubes to Counter Electrodes of Dye-Sensitized Solar Cells. *Chem. Lett.* **2003**, *32*, 28–29.
- (10) Trancik, J. E.; Barton, S. C.; Hone, J. Transparent and Catalytic Carbon Nanotube Films. *Nano Lett.* **2008**, *8*, 982–987.
- (11) Roy-Mayhew, J. D.; Bozym, D. J.; Punckt, C.; Aksay, I. A. Functionalized Graphene as a Catalytic Counter Electrode in Dye-Sensitized Solar Cells. *ACS Nano* **2010**, *4*, 6203–6211.
- (12) Roy-Mayhew, J. D.; Boschloo, G.; Hagfeldt, A.; Aksay, I. A. Functionalized Graphene Sheets as a Versatile Replacement for Platinum in Dye-Sensitized Solar Cells. *ACS Appl. Mater. Interfaces* **2012**, *4*, 2794–2800.
- (13) Jang, H.-S.; Yun, J.-M.; Kim, D.-Y.; Park, D.-W.; Na, S.-I.; Kim, S.-S. Moderately Reduced Graphene Oxide as Transparent Counter Electrodes for Dye-Sensitized Solar Cells. *Electrochim. Acta* **2012**, *81*, 301–307.
- (14) Hsieh, C.-T.; Yang, B.-H.; Chen, Y.-F. Dye-Sensitized Solar Cells Equipped with Graphene-Based Counter Electrodes with Different Oxidation Levels. *Diamond Relat. Mater.* **2012**, *27–28*, 68–75.

- (15) Kavan, L.; Yum, J.-H.; Grätzel, M. Optically Transparent Cathode for Co(III/II) Mediated Dye-Sensitized Solar Cells Based on Graphene Oxide. *ACS Appl. Mater. Interfaces* **2012**, *4*, 6999–7006.
- (16) Wang, H.; Hu, Y. H. Graphene as a Counter Electrode Material for Dye-Sensitized Solar Cells. *Energy Environ. Sci.* **2012**, *5*, 8182–8188.
- (17) Su, C.; Loh, K. P. Carbocatalysts: Graphene Oxide and Its Derivatives. *Acc. Chem. Res.* **2013**, *46*, 2275–2285.
- (18) Kavan, L.; Yum, J.-H.; Grätzel, M. Graphene-Based Cathodes for Liquid-Junction Dye Sensitized Solar Cells: Electrocatalytic and Mass Transport Effects. *Electrochim. Acta* **2014**, *128*, 349–359.
- (19) Fang, B.; Fan, S.-Q.; Kim, J. H.; Kim, M.-S.; Kim, M.; Chaudhari, N. K.; Ko, J.; Yu, J.-S. Incorporating Hierarchical Nanostructured Carbon Counter Electrode into Metal-Free Organic Dye-Sensitized Solar Cell. *Langmuir* **2010**, *26*, 11238–11243.
- (20) Velten, J.; Mozer, A. J.; Li, D.; Officer, D.; Wallace, G.; Baughman, R.; Zakhidov, A. Carbon Nanotube/Graphene Nanocomposite as Efficient Counter Electrodes in Dye-Sensitized Solar Cells. *Nanotechnology* **2012**, *23*, 085201.
- (21) Bard, J. A.; Faulkner, L. R. *Electrochemical Methods*, 2nd ed.; John Wiley & Sons: New York, 2001.
- (22) Menshkykau, D.; Compton, R. G. The Influence of Electrode Porosity on Diffusional Cyclic Voltammetry. *Electroanalysis* **2008**, *20*, 2387–2394.
- (23) Punckt, C.; Pope, M. A.; Liu, J.; Lin, Y.; Aksay, I. A. Electrochemical Performance of Graphene as Effected by Electrode Porosity and Graphene Functionalization. *Electroanalysis* **2010**, *22*, 2834–2841.
- (24) Eng, A. Y. S.; Chua, C. K.; Pumera, M. Intrinsic Electrochemical Performance and Precise Control of Surface Porosity of Graphene-Modified Electrodes Using the Drop-Casting Technique. *Electrochem. Commun.* **2015**, *59*, 86–90.
- (25) Yella, A.; Lee, H.-W.; Tsao, H. N.; Yi, C.; Chandiran, A. K.; Nazeeruddin, M. K.; Diau, E. W.-G.; Yeh, C.-Y.; Zakeeruddin, S. M.; Grätzel, M. Porphyrin-Sensitized Solar Cells with Cobalt (II/III)-Based Redox Electrolyte Exceed 12% Efficiency. *Science* **2011**, *334*, 629–634.
- (26) Li, X. L.; Zhang, G. Y.; Bai, X. D.; Sun, X. M.; Wang, X. R.; Wang, E.; Dai, H. J. Highly Conducting Graphene Sheets and Langmuir-Blodgett Films. *Nat. Nanotechnol.* **2008**, *3*, 538–542.
- (27) Cote, L. J.; Kim, F.; Huang, J. Langmuir-Blodgett Assembly of Graphite Oxide Single Layers. *J. Am. Chem. Soc.* **2009**, *131*, 1043–1049.
- (28) Pope, M. A.; Punckt, C.; Aksay, I. A. Intrinsic Capacitance and Redox Activity of Functionalized Graphene Sheets. *J. Phys. Chem. C* **2011**, *115*, 20326–20334.
- (29) Punckt, C.; Pope, M. A.; Aksay, I. A. On the Electrochemical Response of Porous Functionalized Graphene Electrodes. *J. Phys. Chem. C* **2013**, *117*, 16076–16086.
- (30) Punckt, C.; Pope, M. A.; Aksay, I. A. High Selectivity of Porous Graphene Electrodes Solely Due to Transport and Pore Depletion Effects. *J. Phys. Chem. C* **2014**, *118*, 22635–22642.
- (31) Pope, M. A.; Aksay, I. A. Four-Fold Increase in the Intrinsic Capacitance of Graphene through Functionalization and Lattice Disorder. *J. Phys. Chem. C* **2015**, *119*, 20369–20378.
- (32) Schniepp, H. C.; Li, J. L.; McAllister, M. J.; Sai, H.; Herrera-Alonso, M.; Adamson, D. H.; Prud'homme, R. K.; Car, R.; Saville, D. A.; Aksay, I. A. Functionalized Single Graphene Sheets Derived from Splitting Graphite Oxide. *J. Phys. Chem. B* **2006**, *110*, 8535–8539.
- (33) McAllister, M. J.; Li, J.-L.; Adamson, D. H.; Schniepp, H. C.; Abdala, A. A.; Liu, J.; Herrera-Alonso, M.; Milius, D. L.; Car, R.; Prud'homme, R. K.; Aksay, I. A. Single Sheet Functionalized Graphene by Oxidation and Thermal Expansion of Graphite. *Chem. Mater.* **2007**, *19*, 4396–4404.
- (34) Bagri, A.; Mattevi, C.; Acik, M.; Chabal, Y. J.; Chhowalla, M.; Shenoy, V. B. Structural Evolution During the Reduction of Chemically Derived Graphene Oxide. *Nat. Chem.* **2010**, *2*, 581–587.
- (35) Zhang, C.; Dabbs, D. M.; Liu, L.-M.; Aksay, I. A.; Car, R.; Selloni, A. Combined Effects of Functional Groups, Lattice Defects, and Edges in the Infrared Spectra of Graphene Oxide. *J. Phys. Chem. C* **2015**, *119*, 18167–18176.
- (36) Kudin, K. N.; Ozbas, B.; Schniepp, H. C.; Prud'homme, R. K.; Aksay, I. A.; Car, R. Raman Spectra of Graphite Oxide and Functionalized Graphene Sheets. *Nano Lett.* **2008**, *8*, 36–41.
- (37) Acik, M.; Lee, G.; Mattevi, C.; Pirkle, A.; Wallace, R. M.; Chhowalla, M.; Cho, K.; Chabal, Y. The Role of Oxygen During Thermal Reduction of Graphene Oxide Studied by Infrared Absorption Spectroscopy. *J. Phys. Chem. C* **2011**, *115*, 19761–19781.
- (38) Jung, I.; Field, D. A.; Clark, N. J.; Zhu, Y.; Yang, D.; Piner, R. D.; Stankovich, S.; Dikin, D. A.; Geisler, H.; Ventrice, C. A.; Ruoff, R. S. Reduction Kinetics of Graphene Oxide Determined by Electrical Transport Measurements and Temperature Programmed Desorption. *J. Phys. Chem. C* **2009**, *113*, 18480–18486.
- (39) Bagri, A.; Grantab, R.; Medhekar, N. V.; Shenoy, V. B. Stability and Formation Mechanisms of Carbonyl- and Hydroxyl-Decorated Holes in Graphene Oxide. *J. Phys. Chem. C* **2010**, *114*, 12053–12061.
- (40) Campos-Delgado, J.; Kim, Y. A.; Hayashi, T.; Morelos-Gómez, A.; Hofmann, M.; Muramatsu, H.; Endo, M.; Terrones, H.; Shull, R. D.; Dresselhaus, M. S.; Terrones, M. Thermal Stability Studies of CVD-Grown Graphene Nanoribbons: Defect Annealing and Loop Formation. *Chem. Phys. Lett.* **2009**, *469*, 177–182.
- (41) Dresselhaus, M. S.; Jorio, A.; Hofmann, M.; Dresselhaus, G.; Saito, R. Perspectives on Carbon Nanotubes and Graphene Raman Spectroscopy. *Nano Lett.* **2010**, *10*, 751–758.
- (42) Schwan, J.; Ulrich, S.; Batori, V.; Ehrhardt, H.; Silva, S. R. P. Raman Spectroscopy on Amorphous Carbon Films. *J. Appl. Phys.* **1996**, *80*, 440–447.
- (43) Ferrari, A. C. Raman Spectroscopy of Graphene and Graphite: Disorder, Electron-Phonon Coupling, Doping and Nonadiabatic Effects. *Solid State Commun.* **2007**, *143*, 47–57.
- (44) Kneten, K. R.; McCreery, R. L. Effects of Redox System Structure on Electron-Transfer Kinetics at Ordered Graphite and Glassy Carbon Electrodes. *Anal. Chem.* **1992**, *64*, 2518–2524.
- (45) Liu, L.-M.; Car, R.; Selloni, A.; Dabbs, D. M.; Aksay, I. A.; Yetter, R. A. Enhanced Thermal Decomposition of Nitromethane on Functionalized Graphene Sheets: Ab Initio Molecular Dynamics Simulations. *J. Am. Chem. Soc.* **2012**, *134*, 19011–19016.
- (46) Pantelides, S. T.; Puzyrev, Y.; Tsetseris, L.; Wang, B. Defects and Doping and Their Role in Functionalizing Graphene. *MRS Bull.* **2012**, *37*, 1187–1194.
- (47) Chen, P. H.; McCreery, R. L. Control of Electron Transfer Kinetics at Glassy Carbon Electrodes by Specific Surface Modification. *Anal. Chem.* **1996**, *68*, 3958–3965.
- (48) Perez-Mendoza, M.; Domingo-Garcia, M.; Lopez-Garzon, F. J. Modifications Produced by O-2 and Co2 Plasma Treatments on a Glassy Carbon: Comparison with Molecular Gases. *Carbon* **1999**, *37*, 1463–1474.
- (49) Loh, K. P.; Bao, Q.; Eda, G.; Chhowalla, M. Graphene Oxide as a Chemically Tunable Platform for Optical Applications. *Nat. Chem.* **2010**, *2*, 1015–1024.
- (50) Pumera, M. The Electrochemistry of Carbon Nanotubes: Fundamentals and Applications. *Chem. - Eur. J.* **2009**, *15*, 4970–4978.
- (51) Banks, C. E.; Davies, T. J.; Wildgoose, G. G.; Compton, R. G. Electrocatalysis at Graphite and Carbon Nanotube Modified Electrodes: Edge-Plane Sites and Tube Ends Are the Reactive Sites. *Chem. Commun.* **2005**, 829–841.
- (52) Zhou, M.; Wang, Y.; Zhai, Y.; Zhai, J.; Ren, W.; Wang, F.; Dong, S. Controlled Synthesis of Large-Area and Patterned Electrochemically Reduced Graphene Oxide Films. *Chem. - Eur. J.* **2009**, *15*, 6116–6120.
- (53) Feldt, S. M.; Gibson, E. A.; Gabrielsson, E.; Sun, L.; Boschloo, G.; Hagfeldt, A. Design of Organic Dyes and Cobalt Polypyridine Redox Mediators for High-Efficiency Dye-Sensitized Solar Cells. *J. Am. Chem. Soc.* **2010**, *132*, 16714–16724.
- (54) Pope, M. A.; Korkut, S.; Punckt, C.; Aksay, I. A. Supercapacitor Electrodes Produced through Evaporative Consolidation of Graphene Oxide-Water-Ionic Liquid Gels. *J. Electrochem. Soc.* **2013**, *160*, A1653–A1660.
- (55) Hummers, W. S.; Offeman, R. E. Preparation of Graphitic Oxide. *J. Am. Chem. Soc.* **1958**, *80*, 1339–1339.

(56) Kim, J.; Cote, L. J.; Kim, F.; Yuan, W.; Shull, K. R.; Huang, J. Graphene Oxide Sheets at Interfaces. *J. Am. Chem. Soc.* **2010**, *132*, 8180–8186.

(57) Zhavnerko, G. K.; Agabekov, V. E.; Yaminsky, I. V. Formation of Langmuir Monolayers for AFM Studies by the “Horizontal Precipitation” Method. In *Physics, Chemistry and Application of Nanostructures*; Borisenko, V. E., Filonov, A. B., Gaponenko, S. V., Gurin, V. S., Eds.; World Scientific Publishing Co. Pte. Ltd.: Singapore, 1999; pp 218–220.

(58) Randin, J.-P.; Yeager, E. Differential Capacitance Study on the Basal Plane of Stress-Annealed Pyrolytic Graphite. *J. Electroanal. Chem. Interfacial Electrochem.* **1972**, *36*, 257–276.

(59) Bowler, R.; Davies, T. J.; Hyde, M. E.; Compton, R. G. Electrochemical Cell for Surface Analysis. *Anal. Chem.* **2005**, *77*, 1916–1919.